Acta Crystallographica Section A
Foundations of Crystallography
ISSN 0108-7673

Received 5 September 2011
Accepted 30 November 2011

Image formation in the scanning transmission electron microscope using object-conjugate detectors

C. Dwyer,[a,b,c]* S. Lazar,[d] L. Y. Chang[a,e] and J. Etheridge[a,b]

[a]Monash Centre for Electron Microscopy, Monash University, Victoria 3800, Australia, [b]Department of Materials Engineering, Monash University, Victoria 3800, Australia, [c]ARC Centre of Excellence in the Design of Light Metals, Monash University, Victoria 3800, Australia, [d]FEI Electron Optics, 5600 KA Eindhoven, The Netherlands, and [e]School of Chemistry, Monash University, Victoria 3800, Australia. Correspondence e-mail: christian.dwyer@monash.edu

This work presents a theoretical analysis of image formation in a scanning transmission electron microscope equipped with electron detectors in a plane conjugate to the specimen. This optical geometry encompasses both the three-dimensional imaging technique of scanning confocal electron microscopy (SCEM) and a recently developed atomic resolution imaging technique coined real-space scanning transmission electron microscopy (R-STEM). Image formation in this geometry is considered from the viewpoints of both wave optics and geometric optics, and the validity of the latter is analysed by means of Wigner distributions. Relevant conditions for the validity of a geometric interpretation of image formation are provided. For R-STEM, where a large detector is used, it is demonstrated that a geometric optics description of image formation provides an accurate approximation to wave optics, and that this description offers distinct advantages for interpretation and numerical implementation. The resulting description of R-STEM is also demonstrated to be in good agreement with experiment. For SCEM, it is emphasized that a geometric optics description of image formation is valid provided that higher-order aberrations can be ignored and the detector size is large enough to average out diffraction from the angle-limiting aperture.

1. Introduction

The last decade has witnessed several significant advances in transmission electron microscope instrumentation. Most notable of these advances is the advent of commercially available multipole electron-optical elements which compensate the inherent spherical aberration of conventional electron lenses (Haider *et al.*, 1998; Krivanek *et al.*, 1999). Such 'aberration correctors' can be fitted to the objective postfield and/or the objective prefield of a transmission electron microscope, giving rise to significantly improved resolution in fixed-beam imaging techniques and scanning transmission electron microscopy (STEM) imaging techniques, respectively. Instruments equipped with both prefield and postfield aberration correctors, coined 'double-aberration-corrected' instruments, are now available. In addition to the improvement of existing imaging techniques, such instruments afford the exploration of new, previously unfeasible or restricted, optical geometries capable of accessing new information about the specimen. Examples include the three-dimensional imaging technique of scanning confocal electron microscopy (SCEM) (Frigo *et al.*, 2002; Nellist *et al.*, 2006; Takeguchi *et al.*, 2008) and, very recently, probe imaging (Etheridge *et al.*, 2011) and real-space STEM (R-STEM) imaging (Etheridge *et al.*, 2011; Lazar *et al.*, 2011).

From a theoretical perspective, new optical geometries often entail new challenges in terms of image simulation and interpretation. In the present work, we consider image formation in a STEM geometry with the electron detector placed in a plane conjugate to the object (as distinct from the diffraction plane used in conventional STEM). This geometry includes both SCEM and R-STEM, the former employing a small axial disc detector, and the latter employing large axial disc and large annular detectors. The latter technique, in particular, is still in its infancy and remains to be fully explored. The technique has been demonstrated (Lazar *et al.*, 2011) to give rise to incoherent atomic resolution images in a manner similar to conventional high-angle annular dark-field (ADF) STEM (Pennycook & Boatner, 1988; Loane *et al.*, 1992; Nellist & Pennycook, 2000) and it has been recently utilized in probe imaging experiments (Etheridge *et al.*, 2011) to provide a reference image for locating the probe position.

One of the main developments of the present work is a mathematical description of the R-STEM imaging mechanism,

thus providing a more solid foundation for image interpretation and future developments and applications of the technique. As will be demonstrated, the R-STEM imaging mechanism provides a rather beautiful example of how, under appropriate circumstances, a wave optics (or quantum mechanical) theory of image formation reduces to a geometric optics (or classical) one. In a practical sense, the geometric optics approximation also offers clear advantages in terms of interpretation and numerical implementation. (To avoid any potential confusion, we emphasize here that the considerations of wave *versus* geometric optics are applied to the image formation and detection processes, and that electron scattering by the specimen is always treated quantum mechanically.) Although for reasons that are different to the R-STEM case, the geometric optics approximation is shown to be applicable to aberration-corrected SCEM provided that the detector is large enough to average out diffraction from the angle-limiting aperture. The theoretical analysis given here provides a formal reconciliation of wave and geometric optics interpretations of SCEM found in recent literature (Mitsuishi *et al.*, 2010; Wang *et al.*, 2011).

The layout of this article is as follows. §2 provides a description of the relevant optical configurations. §3 presents a wave optics formulation of STEM imaging using object-conjugate detectors and discusses the difficulties associated with a numerical implementation for R-STEM. In §4, a more tractable approach to R-STEM is presented based on geometric optics. This approach is compared with the wave optics approach and experiment, and some aspects of the experimental setup required for R-STEM are discussed. §5 examines the formal relationship between the wave and geometric optics descriptions of STEM imaging with object-conjugate detectors, and discusses the requirements for the validity of the geometric optics approximation in relation to both R-STEM and SCEM. Conclusions are presented in §6.

2. Electron-optical geometry

Fig. 1 depicts the experimental geometry considered in the present work. The electron-optical configuration is a scanning confocal geometry: the electron-transparent specimen resides in a plane which is simultaneously (i) the image plane of the objective prefield with respect to the electron source, and (ii) the object plane of the objective postfield with respect to the image plane. Hence the focused electron beam, which is raster-scanned across the specimen by the upper beam deflectors, is maintained in focus at the image plane. An electron detector is situated in the image plane. For SCEM, the detector is a small axial disc, and for R-STEM it is a large axial disc or a large annular detector (the terms 'small' and 'large' will be qualified below). As the beam is scanned across the specimen its position on the detector is kept stationary. In some SCEM experiments this has been achieved by actually translating the specimen instead of raster-scanning the beam, whereas in the recent R-STEM experiments this was achieved by an appropriate use of upper and lower beam deflectors. The detector output is synchronized with the scanning beam, so that the detector signal as a function of the beam position on the specimen constitutes the final image. For SCEM, a crucial additional step is to acquire images for different heights of the specimen with respect to the confocal plane, enabling the extraction of three-dimensional information about the specimen.

The relative size and geometry of the electron detector are, among other important factors, crucial in determining the nature of the final image. For SCEM, the detector is ideally a pinhole in order to maximize depth sensitivity (signal-to-noise requirements aside). In recent aberration-corrected SCEM experiments (Wang *et al.*, 2011) the detector size was, after scaling to the relevant magnification, a few tenths of a nanometre. For R-STEM, the generation of incoherent atomic resolution images requires that the detector is significantly larger than the transverse extent of the ideal, that is, aberration-free, image-plane intensity. In recent R-STEM experiments (Etheridge *et al.*, 2011; Lazar *et al.*, 2011) the dimensions of the detectors, scaled to the relevant magnification, ranged from several nanometres up to several thousand nanometres.

Aberrations introduced by the objective postfield can significantly affect the image-plane intensity. In SCEM, the

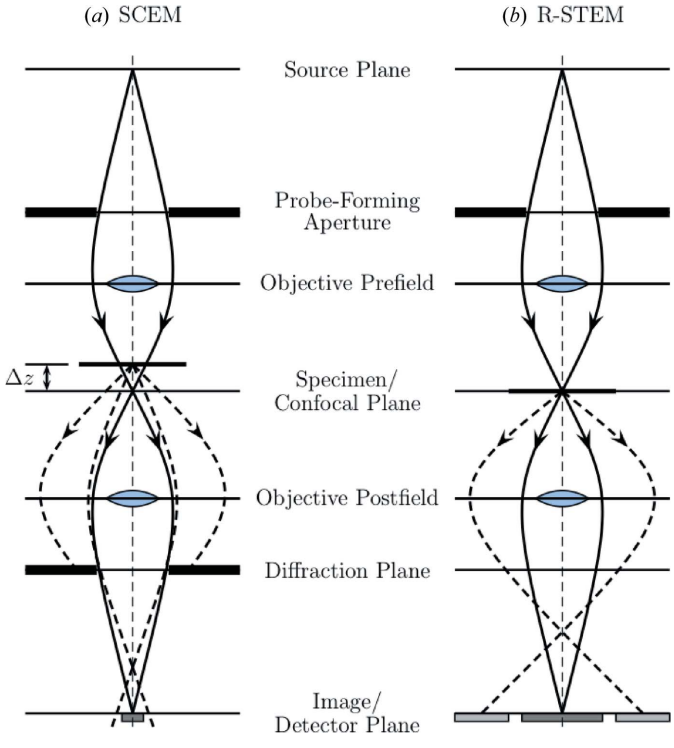

Figure 1
STEM imaging with object-conjugate detectors. In SCEM (*a*), a small axial detector has the effect of excluding electrons scattered by the specimen (represented by dashed rays) when the specimen is moved out of the confocal plane, giving rise to depth sensitivity; an aperture is employed in the diffraction plane to circumvent the higher-order postfield aberrations experienced by electrons scattered by the specimen to large angles. In R-STEM (*b*), electrons scattered to large angles experience strong postfield aberrations, resulting in a significant displacement of these electrons from the ideal image point; these electrons are collected by the large annular detector.

effects of higher-order postfield aberrations are detrimental, and they can be circumvented by employing an angle-limiting aperture in the diffraction plane.

In R-STEM, the higher-order postfield aberrations are, in fact, crucial in determining the image contrast. This has been demonstrated by a comparison of experimental images taken with and without angle-limiting apertures in the diffraction plane. Hence, apart from the usual factors which must be included in a theory of conventional STEM imaging (*i.e.* descriptions of the electron probe, scattering of this probe by the specimen and the detection of intensity), a theory of R-STEM imaging must also incorporate the effects of higher-order postfield aberrations. In the present work, the incorporation of these aberrations is presented using both wave optics and geometric optics. As will be shown, in the case of R-STEM the rigour of wave optics is counterbalanced by computational challenges in its implementation. A geometric optics approach, on the other hand, provides both sufficient accuracy and the computational feasibility necessary for image simulation.

3. Wave optics theory

We will initially outline how quantum mechanics is used to calculate electron scattering by the specimen in the STEM geometry. This step will be assumed in both the wave and geometric optics approaches to image formation presented below. Various methods exist for calculating the relevant electron scattering. For example, multislice (Goodman & Moodie, 1974; Kirkland *et al.*, 1987; Ishizuka, 2002; Stadelmann, 2004) and Bloch-state (Allen *et al.*, 2003; Findlay *et al.*, 2003; Rossouw *et al.*, 2003; Stadelmann, 2004) approaches are common. For definiteness, we summarize these approaches below. We use a 'crystallographic convention' for plane waves and Fourier transformations, where the magnitude of the incident electron's total wavevector is equal to $1/\lambda$, where λ is the wavelength. We use bold symbols to denote two-dimensional vectors transverse to the optic axis. Points in the specimen and image planes will generally be denoted by $\mathbf{x}$, while points in the diffraction plane will generally be denoted by a reciprocal-space vector $\mathbf{k}$. The actual (real-space) position in the diffraction plane of a lens is related to $\mathbf{k}$ by $\lambda f\mathbf{k}$, where f is the lens focal length.

Using a paraxial approximation to Schrödinger quantum mechanics, the wavefunction at a point $\mathbf{k}$ in the diffraction plane arising from a focused electron probe positioned at the point $\mathbf{x}_0$ at the specimen entrance surface can be written in the form (Dwyer, 2010)

$$\tilde{\psi}(\mathbf{k}, \mathbf{x}_0) = \int \mathrm{d}^2\mathbf{k}_0\, iG(\mathbf{k}, \mathbf{k}_0)\tilde{\psi}_0(\mathbf{k}_0)\exp(-2\pi i\mathbf{k}_0 \cdot \mathbf{x}_0), \qquad (1)$$

where $\tilde{\psi}_0(\mathbf{k})$ is the electron wavefunction in the plane of the probe-forming aperture corresponding to a probe centred at the origin of the entrance surface, and $G(\mathbf{k}, \mathbf{k}_0)$ is the momentum-space propagator which incorporates any elastic scattering caused by the specimen. Thermal diffuse scattering, which is important in the present context since it dominates at large scattering angles, is accommodated here using the frozen-phonon approach (Loane *et al.*, 1991; Kirkland, 2010). Other forms of inelastic scattering are not considered in the present work. The effects of objective prefield aberrations are implicitly incorporated into $\tilde{\psi}_0$. In the present work, knowledge of the wavefunction in either the specimen exit surface or the diffraction plane (the two being related by Fourier transformation up to an unimportant phase factor) will be assumed when necessary.

In the case of conventional STEM imaging, which uses a detector in the diffraction plane, the STEM image intensity for probe position $\mathbf{x}_0$ is computed as an integral of $|\tilde{\psi}(\mathbf{k}, \mathbf{x}_0)|^2$ over points $\mathbf{k}$ lying on the detector. Such approaches to STEM image simulations are now well established and routinely carried out on desktop computers (Kirkland, 2010; Dwyer, 2010).

For the present optical geometry, we must compute the intensity on the detector in the image plane. To this end, a wave optics approach to image formation seems a natural choice, especially from the viewpoint of workers familiar with existing theories of atomic resolution transmission electron microscopy (TEM) and STEM imaging. In this approach, the effects of objective postfield aberrations are incorporated as phase shifts in the diffraction plane (assuming validity of the isoplanatic approximation), and the wavefunction in the image plane is computed explicitly as an intermediate step in calculating the detected intensity. The wavefunction at a point $\mathbf{x}$ in the image plane can be written in the form

$$\begin{aligned}\psi_i(\mathbf{x}, \mathbf{x}_0) &= \int \mathrm{d}^2\mathbf{k}\, \tilde{\psi}(\mathbf{k}, \mathbf{x}_0)\exp[-2\pi i\chi(\mathbf{k})]\exp[2\pi i\mathbf{k} \cdot (\mathbf{x}_0 + \mathbf{x})] \\ &= \int \mathrm{d}^2\mathbf{k}\, \mathrm{d}^2\mathbf{k}_0\, iG(\mathbf{k}, \mathbf{k}_0)\tilde{\psi}_0(\mathbf{k}_0) \\ &\quad \times \exp[-2\pi i\chi(\mathbf{k})]\exp(2\pi i\mathbf{k} \cdot \mathbf{x})\exp[2\pi i(\mathbf{k} - \mathbf{k}_0) \cdot \mathbf{x}_0], \end{aligned} \qquad (2)$$

where $-2\pi\chi(\mathbf{k})$ and $2\pi\mathbf{k} \cdot \mathbf{x}_0$ are the phase shifts due to postfield aberrations and descan, respectively. Introducing a detector function $D(\mathbf{x})$ which equals unity (zero) for points $\mathbf{x}$ lying on (off) the detector, the final image intensity for probe position $\mathbf{x}_0$ can be written in the form

$$I(\mathbf{x}_0) = \int \mathrm{d}^2\mathbf{x}\, D(\mathbf{x})|\psi_i(\mathbf{x}, \mathbf{x}_0)|^2, \qquad (3)$$

where $\psi_i(\mathbf{x}, \mathbf{x}_0)$ is computed according to equation (2). Since equation (3) makes no assumptions regarding the detector geometry, it is applicable to both SCEM and R-STEM.

A numerical implementation of the above formulation involves essentially only one additional step with respect to conventional STEM, namely, the incorporation of postfield aberrations. However, to ensure accuracy in the calculation, the aberration function must be adequately sampled at all points $\mathbf{k}$ in the diffraction plane for which $\tilde{\psi}(\mathbf{k}, \mathbf{x}_0)$ has an appreciable value. In the case of SCEM, where an angle-limiting aperture is employed, the effect of higher-order aberrations is not dominant and no difficulty arises. In the case of R-STEM, however, no such aperture is employed, so that electrons scattered to large angles can contribute to the image intensity. In this case, the higher-order postfield aberrations are crucial in determining how the intensity is distributed

across the detector. Achieving sufficient sampling of the aberration function at all relevant points of the diffraction plane then presents a difficulty.

To explore this difficulty in more detail, we adopt a common aberration notation (Uhlemann & Haider, 1998) and consider the (negative of the) phase shift associated with the nth-order round term (n = odd) in the aberration function:

$$\varphi_n(\mathbf{k}) = \frac{2\pi}{n+1} C_n \lambda^n |\mathbf{k}|^{n+1}. \tag{4}$$

The variation of this phase shift with respect to a small increase in the length of $\mathbf{k}$ is, to leading order,

$$\Delta\varphi_n \simeq \frac{\partial \varphi_n}{\partial \mathbf{k}} \Delta\mathbf{k} = 2\pi C_n \lambda^n |\mathbf{k}|^n |\Delta\mathbf{k}|. \tag{5}$$

For a sampling scheme consistent with the use of the fast Fourier transform (Press *et al.*, 2002), we have that $|\Delta\mathbf{k}| = 1/a$, where a is the size of the supercell used (implicitly or explicitly) in the simulation. We also have that the maximum scattering vector is $|\mathbf{k}_{\max}| = N/2a$, where N is the number of pixels along a. Hence the following condition is obtained for sampling the aberration function above the Nyquist limit at $\mathbf{k}_{\max}$:

$$\Delta\varphi_n = \frac{2\pi C_n \lambda^n (N/2a)^n}{a} = \frac{2\pi C_n \lambda^n N^n}{2^n a^{n+1}} < \pi. \tag{6}$$

Rearranging, the lower limit on the supercell size is given by

$$a > 2C_n \lambda^n \left(\frac{N}{2a}\right)^n = 2C_n \beta_{\max}^n, \tag{7}$$

where $\beta_{\max}$ is the maximum scattering angle in the calculation. (As a point of later relevance, this lower limit on the supercell size is entirely consistent with the displacement of a geometric ray from the ideal image point, which is given by $C_n\beta^n$). To see the implications of the above, consider a calculation involving a fifth-order spherical aberration coefficient C_5 = 10 mm [a value representative of higher-order aberrations in a third-order spherical aberration C_3-corrected objective postfield (Chang *et al.*, 2006)] and a maximum scattering angle $\beta_{\max} \simeq 100$ mrad (a value representative of that required to encompass the large-angle scattering in a transmission electron microscope). Substituting these values into equation (7) gives $a \gtrsim 200$ nm, which is approximately 100 times larger than supercells typically used for simulations of conventional atomic resolution STEM images. The implied array size N^2, where $N = 2a|\mathbf{k}_{\max}|$, is then 10^4 times larger than that typically used and will likely exhaust the memory capacity of current desktop computers. For the case of a C_3-dominated postfield, assuming $C_3 = 1$ mm, we obtain that $a \gtrsim 2000$ nm, so that the implied array size is even larger.

From the above considerations it is evident that a direct and, what will appear in retrospect, naive application of wave optics to incorporate the higher-order postfield aberrations in R-STEM places excessive demands on computational resources.

4. Geometric optics theory of R-STEM

As an alternative to computing the R-STEM image intensity *via* explicit calculation of the image wavefunction, geometric optics can be used to compute how the intensity in the image plane is displaced with respect to the ideal (aberration-free) image. Hence, from such computations, the intensity lying on the detector can be inferred. This section provides a brief derivation of this geometric optics approach, with many steps omitted for ease of reading. The validity of such an approach is ensured provided that the detector constitutes a large portion of the image plane, so that interference effects are averaged out. Questions of validity are considered in detail in §5, where a more rigorous derivation of the geometric optics description is presented.

Under the isoplanatic approximation, the aberration-induced displacement of a geometric ray from its ideal image point depends only on the angle at which the ray leaves the object plane. If the spatial extent of the ideal image is small in comparison to the aberration-induced displacements, then the spatial extent of the ideal image can be neglected, and the position of the ray in the image plane is approximately equal to the ray displacement itself (see Fig. 2). Ignoring the possibility of image inversion, the displacement of a ray leaving the object plane in the direction corresponding to $\mathbf{k}$ is given by

$$\mathbf{x}(\mathbf{k}) = \nabla\chi(\mathbf{k}), \tag{8}$$

where the gradient is taken with respect to $\mathbf{k}$. Hence, under the stated assumptions, the position of a ray in the image plane is $\mathbf{x}(\mathbf{k})$. The appropriate weight of each ray is given by the intensity of the wavefield in the diffraction plane multiplied by the inverse of the Jacobian determinant. (Inclusion of the Jacobian determinant ensures that the total intensity is conserved from one optical plane to the next). Hence, for a probe at position $\mathbf{x}_0$, the image-plane intensity can be written in the form

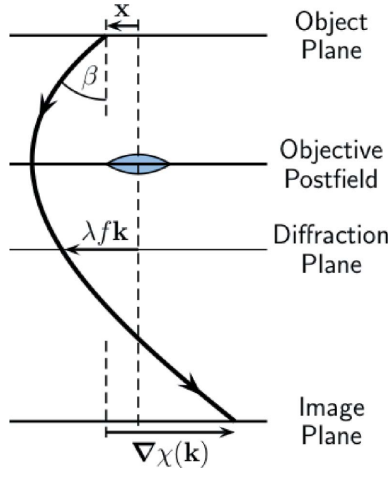

Figure 2
The aberration-induced displacement of a ray that leaves the object plane in the direction of β (or, equivalently, the direction corresponding to $\mathbf{k}$). If the spatial extent of the aberration-free image is small (that is, if $|\mathbf{x}|$ can be regarded as small), then the position of the ray in the image plane will be approximately equal to the displacement $\nabla\chi(\mathbf{k})$.

$$I(\mathbf{x}, \mathbf{x}_0) \simeq |J|^{-1} |\tilde{\psi}(\mathbf{k}(\mathbf{x}), \mathbf{x}_0)|^2, \quad (9)$$

where $\mathbf{k}(\mathbf{x})$ is the inverse of the function $\mathbf{x}(\mathbf{k})$ and $|J|$ is the determinant of the Jacobian matrix associated with the transformation $\mathbf{x}(\mathbf{k}) : \mathbf{k} \rightarrow \mathbf{x}$. Substituting equation (9) into equation (3), the R-STEM image intensity can be written in the form

$$I_{\text{R-STEM}}(\mathbf{x}_0) \simeq \int \mathrm{d}^2\mathbf{x}\, D(\mathbf{x}) |J|^{-1} |\tilde{\psi}(\mathbf{k}(\mathbf{x}), \mathbf{x}_0)|^2. \quad (10)$$

While equation (10) may appear satisfactory, it suffers from severe complications arising from any multivaluedness of $\mathbf{k}(\mathbf{x})$, *e.g.* when focal points or caustics are present in the image plane. However, these complications can be eliminated by making a change of integration variable from $\mathbf{x}$ to $\mathbf{k}$, in which case the Jacobian determinant cancels out, and a satisfactory expression for the R-STEM image intensity is obtained in the form

$$I_{\text{R-STEM}}(\mathbf{x}_0) \simeq \int \mathrm{d}^2\mathbf{k}\, D(\mathbf{x}(\mathbf{k})) |\tilde{\psi}(\mathbf{k}, \mathbf{x}_0)|^2. \quad (11)$$

Equation (11) provides a very convenient description of R-STEM imaging: the function $D(\mathbf{x}(\mathbf{k}))$ can be interpreted as describing an *effective* detector operating in the diffraction plane. With this interpretation, equation (11) is formally equivalent to that for conventional STEM imaging, except that the shape of the effective detector is determined not only by the detector geometry, but also by the objective postfield aberrations. Hence the effects of postfield aberrations constitute a crucial difference between the conventional STEM and R-STEM imaging modes.

In addition to its simple interpretation, equation (11) also offers a distinct advantage in terms of image simulations: given the aberration coefficients of the objective postfield, the effective detector function $D(\mathbf{x}(\mathbf{k}))$ is easily computed. Then all that is required to compute the R-STEM intensity for a given probe position is the scattered intensity in the diffraction plane, which is readily obtained using a multislice or Bloch-state approach to conventional STEM images. In this manner, the simulation of R-STEM images poses no greater difficulty than the simulation of conventional STEM images.

4.1. Comparison of geometric theory of R-STEM and experiment

As an initial test of the geometric optics theory of R-STEM, Fig. 3 compares experimental and simulated R-STEM images of [001] $SrTiO_3$. This specimen was chosen because it contains both light (oxygen) and moderately heavy (strontium) atoms. The experimental images were acquired using a Titan^3 80–300 microscope (FEI Co.) equipped with objective prefield and postfield spherical aberration correctors (CEOS GmbH) and operating at 200 kV. The microscope was equipped with a descan system that maintains a stationary beam in the image plane as the probe is raster-scanned across the specimen. The probe convergence semi-angle was approximately 20.5 mrad, and the images were acquired using a disc image-plane detector of radius 3.9 nm, and an annular image-plane detector with inner and outer radii of 15 and 93 nm (these detectors were operated simultaneously). Convergent-beam electron diffraction was used to measure the approximate thickness of the sample to an accuracy of about ±3 nm. The simulations in Fig. 3(*a*) were performed using the geometric optics theory for parameters matching the experimental conditions. The simulations assume an aberration-free objective prefield, and objective postfield aberrations of $C_5 = 6.8$ mm, $|A_5| = 3.1$ mm and $C_7 = 197$ mm (values representative of higher-order aberrations in a C_3-corrected objective postfield). The shapes of the effective detectors under these conditions are shown in Fig. 3(*b*). The electron

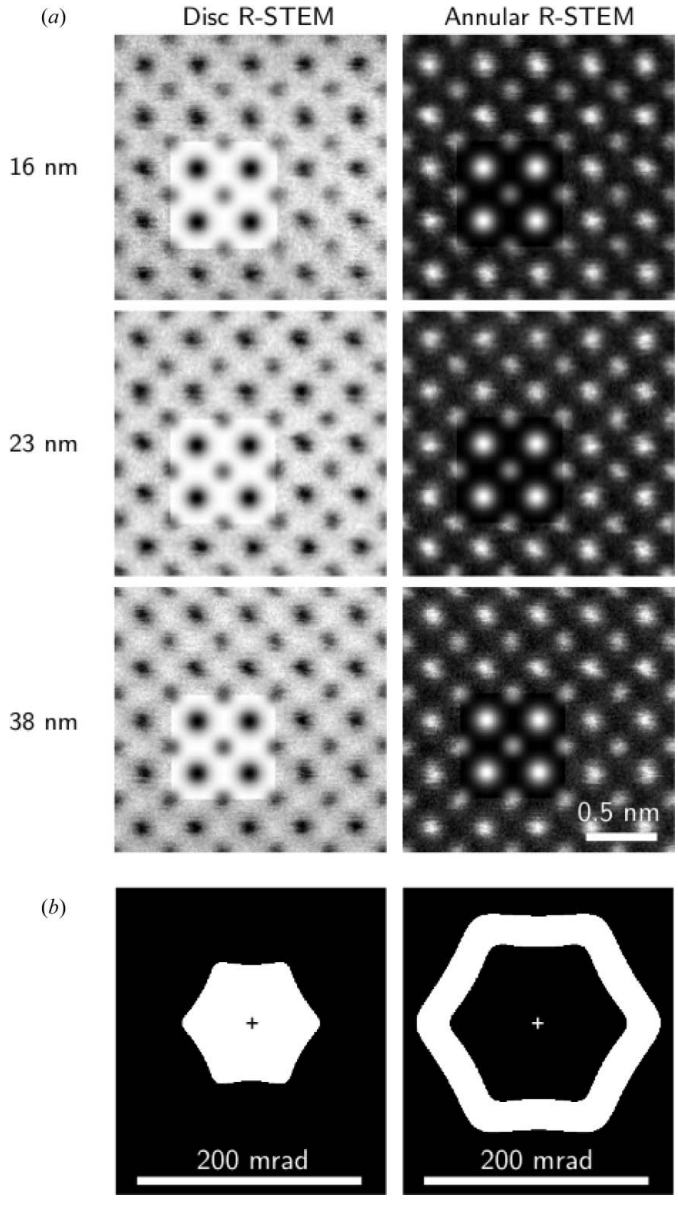

Figure 3
(*a*) Comparison of experimental disc and annular R-STEM images of [001] $SrTiO_3$ and simulations based on the geometric optics theory (inset of each image). The approximate experimental thickness of the sample is indicated on the left. All images are displayed such that the minimum and maximum intensities correspond to black and white, respectively. (*b*) The shape of the effective disc and annular detectors operating in the diffraction plane. The apparent hexagonal shapes are caused by the A_5 aberration. Crosses mark the centre of the diffraction plane.

scattering portion of the simulations was performed using a modified frozen-phonon multislice code adapted for speed to run on the general-purpose graphics processing unit (GPGPU) (Dwyer, 2010). On account of the interpretation of R-STEM in terms of an effective detector, the important effects that arise in conventional STEM from the partial spatial coherence of the incident electron beam (source size effects) (Dwyer *et al.*, 2008, 2010; LeBeau *et al.*, 2008; Maunders *et al.*, 2011) are manifest in R-STEM in the same manner. These effects have been included qualitatively here by convoluting with a Gaussian function of 0.1 nm full width at half-maximum (FWHM). The effects of partial temporal coherence (prefield focal fluctuations) are relatively unimportant (Dwyer *et al.*, 2010) and have been ignored. The supercell used for the electron scattering portion of the simulations was 3.1 × 3.1 nm (8 × 8 unit cells of [001] $SrTiO_3$), sampled using a 512 × 512 array. The same supercell was used for the imaging portion of the simulation.

From Fig. 3(*a*) it is seen that the experimental disc R-STEM images exhibit all the qualities of an incoherent bright-field image, that is, intensity minima located at the positions of atomic columns, with deeper minima located at the sites of columns with greater atomic number. In an analogous manner, the annular R-STEM images exhibit all the qualities of an incoherent dark-field image, that is, a conventional ADF image. The image contrast in disc R-STEM is approximately complementary to that in annular R-STEM. These observations are consistent with the shapes of the effective detectors operating in the diffraction plane (Fig. 3*b*): the large effective disc detector approximately fills the hole in the effective annular detector, giving rise to an incoherent bright-field image. The contrast of the experimental images shows remarkably little change over the thickness range indicated. In fact, the only change with respect to thickness that is discernible in the experimental images in Fig. 3(*a*) occurs between those taken at thicknesses 16 and 23 nm, where the contrast of the Ti—O columns appears slightly fainter in the thinner specimen. Nonetheless, these subtle changes in contrast are reproduced by the simulations and can be attributed to electron channelling. Although it is not apparent from the greyscale of the images in Fig. 3(*a*), the overall intensities in the experimental disc and annular R-STEM images exhibit an obvious decrease and increase with thickness, respectively, as is consistent with the calculations discussed in §4.2. Hence, we find that the overall qualitative agreement between experimental and simulated images is very good. This agreement supplements that reported earlier (Lazar *et al.*, 2011) for images of LaB_6 and provides substantial confidence in the geometric optics theory of R-STEM image formation described above.

We conclude this subsection with some remarks regarding the experimental setup required for R-STEM. The experimental images reported here and in our earlier works (Etheridge *et al.*, 2011; Lazar *et al.*, 2011) were acquired using instruments equipped with both an aberration-corrected objective prefield and an aberration-corrected postfield. The correction of prefield aberrations enables the formation of a significantly smaller electron probe, leading directly to an increase in the resolution of R-STEM images. On the other hand, correction of the postfield aberrations does not influence the resolution of the images and is not a requirement for the acquisition of R-STEM images. The postfield aberrations do, however, influence the geometry of the effective detector operating in the diffraction plane, as discussed above. To examine this influence further, Fig. 4 shows the correspondence between the scattering angle and the image-plane displacement for sets of aberration coefficients that are representative of C_3-dominated and C_3-corrected objective postfields. While this figure ignores non-round aberrations, it is nonetheless useful for determining the approximate scattering angles applicable to a particular R-STEM experiment. For example, the upper solid curve applies to the instruments used here and in our previous works (Etheridge *et al.*, 2011; Lazar *et al.*, 2011). On these instruments the (effective) image-plane displacement corresponding to the inner edge of the annular detector can be varied from 15 to 2300 nm, so that the inner collection angle can be varied from approximately 70 to 170 mrad. On similar instruments without a postfield aberration corrector, to which the lower solid curve in Fig. 4 applies, the inner collection angle can be varied from approximately 30 to 120 mrad. Since the latter range, with its smaller inner angles, enables an increased signal in the annular images, the presence of significant C_3 aberration would be beneficial in this sense.

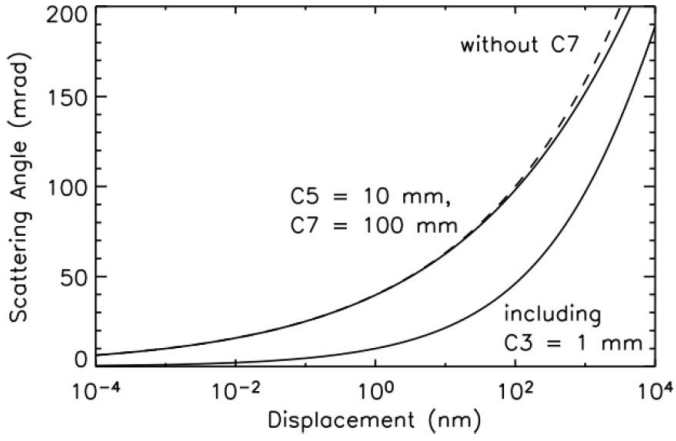

Figure 4
The scattering angles corresponding to image-plane displacements for sets of aberration coefficients applicable to C_3-dominated and C_3-corrected objective postfields. Aberration coefficients other than those indicated are set to zero. The graph applies to all beam energies.

4.2. Comparison of wave and geometric theories of R-STEM

As a quantitative comparison of the wave and geometric approaches to R-STEM in a practical scenario, Fig. 5 shows a comparison of intensities in line profiles across the [110] direction of the [001]-oriented $SrTiO_3$ unit cell for selected thicknesses up to 80 nm. These simulations assumed a beam energy of 300 keV and convergence semi-angle of 17 mrad. In order to enable a tractable wave optics calculation, the outer radius of the annular detector was reduced to 25 nm in both

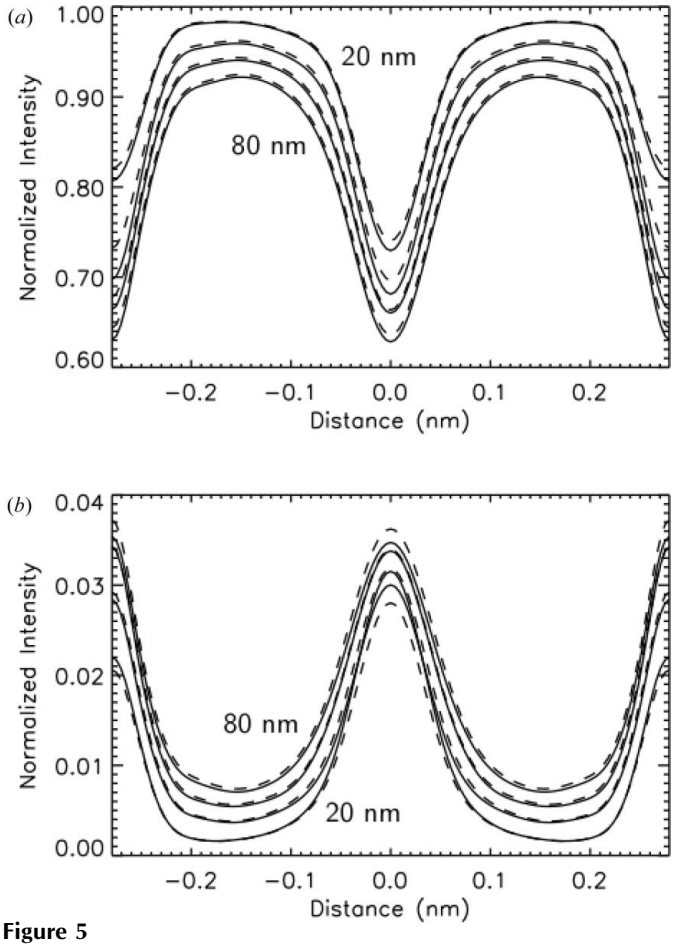

Figure 5
Quantitative comparison of wave (solid lines) and geometric optics (dashed lines) simulations of (*a*) disc and (*b*) annular R-STEM images of [001]-oriented $SrTiO_3$. The intensities correspond to diagonal line traces across the projected unit cell, with Sr at the centre. Data are shown for sample thicknesses of 20, 40, 60 and 80 nm.

calculations. The supercell used for the imaging portion of the wave optics simulation was 50 × 50 nm (128 × 128 unit cells of [001] $SrTiO_3$), sampled using a 8192 × 8192 array. All other parameters are essentially unchanged from those in Fig. 3. The results in Fig. 5 confirm that the geometric optics approximation is in excellent quantitative agreement with the wave optics results, with a largest relative error of about 5% under the stated conditions.

5. Analysis of the geometric optics limit

This section examines the formal relationship between the wave and geometric optics descriptions of STEM imaging using object-conjugate detectors. The geometric optics description emerges as an appropriate limit to the wave optics theory. Hence the benefit of the present considerations lies in providing a clearer assessment of the validity of the geometric optics description for R-STEM and SCEM. In addition, the manner in which the wave optics theory reduces to the geometric optics one constitutes an interesting and worthwhile study in its own right.

We begin with the complete wave optics description, but couched in a slightly different form which is more suited to the present considerations. For clarity, it will be assumed temporarily that the probe is centred at the origin of the specimen entrance surface so that the probe position $\mathbf{x}_0$ can be omitted (dependence on the probe position will be restored later).

The intensity at a point $\mathbf{x}$ in the image plane is given by $|\psi_i(\mathbf{x})|^2$, where ψ_i is the (aberrated) wavefunction in the image plane. As described earlier, ψ_i can be written as the inverse Fourier transform of the wavefunction in the diffraction plane $\tilde{\psi}$ multiplied by the aberration phase shift:

$$\psi_i(\mathbf{x}) = \int \mathrm{d}^2\mathbf{k}\, \tilde{\psi}(\mathbf{k}) \exp[-2\pi i \chi(\mathbf{k})] \exp(2\pi i \mathbf{k}\cdot\mathbf{x}). \qquad (12)$$

Equation (12) can be interpreted as an overlap integral in Fourier space involving the wavefunction $\tilde{\psi}(\mathbf{k})$ and a 'conjugate' wavefunction

$$\tilde{\psi}^*_{\mathrm{D}}(\mathbf{k},\mathbf{x}) = \exp[-2\pi i \chi(\mathbf{k})] \exp(2\pi i \mathbf{k}\cdot\mathbf{x}), \qquad (13)$$

which originates from a point $\mathbf{x}$ on the detector (Kainuma, 1955). As before, the detected intensity is given by integrating over the detector in the image plane:

$$\begin{aligned} I &= \int \mathrm{d}^2\mathbf{x}\, D(\mathbf{x}) \left| \int \mathrm{d}^2\mathbf{k}\, \tilde{\psi}^*_{\mathrm{D}}(\mathbf{k},\mathbf{x}) \tilde{\psi}(\mathbf{k}) \right|^2 \\ &= \int \mathrm{d}^2\mathbf{x}\, D(\mathbf{x}) \int \mathrm{d}^2\mathbf{k}\, \mathrm{d}^2\mathbf{k}'\, \tilde{\psi}_{\mathrm{D}}(\mathbf{k},\mathbf{x}) \tilde{\psi}^*(\mathbf{k}) \tilde{\psi}^*_{\mathrm{D}}(\mathbf{k}',\mathbf{x}) \tilde{\psi}(\mathbf{k}'). \end{aligned} \qquad (14)$$

The last equality is significant because it can be interpreted as the overlap of two density matrices, one describing the pure quantum state of the scattered electron probe and the other describing the *mixed* quantum state associated with the objective postfield and detector portion of the optical geometry. The former will be called the 'probe' state, while the latter will be called the 'detector' state.

For the present purposes, it is convenient to describe the probe and detector states using a formalism that explicitly accommodates mixed states. While the density matrix formalism is well known for this ability and has been used to describe electron scattering in TEM (Schattschneider *et al.*, 1999; Verbeeck *et al.*, 2009), here we use a formalism based on Wigner distributions (Castano, 1989; Bastiaans, 1997; Torre, 2005), as it accommodates mixed states and allows a more vivid analysis of the geometric optics limit (Berry, 1977). A Wigner distribution $W(\mathbf{x},\mathbf{k})$ describes the state of a quantum particle in terms of a position coordinate $\mathbf{x}$ and a wavevector (or momentum) coordinate $\mathbf{k}$, *i.e.* $\mathbf{x}$ and $\mathbf{k}$ taken together denote a point in phase space. Essentially, the value of $W(\mathbf{x},\mathbf{k})$ can be considered as the strength of a geometric ray at $\mathbf{x}$ moving in direction $\mathbf{k}$, but with the important caveats that (i) physically realisable states consist of a *distribution* of such rays consistent with the Heisenberg uncertainty principle, and (ii) the strength of a given ray can be *negative*.

The Wigner distributions of the probe and detector states can be written in the forms

$$W(\mathbf{x},\mathbf{k}) = \int \mathrm{d}^2\mathbf{k}'\, \tilde{\psi}^*(\mathbf{k}-\mathbf{k}'/2)\,\tilde{\psi}(\mathbf{k}+\mathbf{k}'/2)\exp(2\pi i\mathbf{k}'\cdot\mathbf{x}), \tag{15}$$

and

$$W_{\mathrm{D}}(\mathbf{x},\mathbf{k}) = \int \mathrm{d}^2\mathbf{x}'\, D(\mathbf{x}') \int \mathrm{d}^2\mathbf{k}'\, \tilde{\psi}^*_{\mathrm{D}}(\mathbf{k}-\mathbf{k}'/2,\mathbf{x}') \times \tilde{\psi}_{\mathrm{D}}(\mathbf{k}+\mathbf{k}'/2,\mathbf{x}')\exp(2\pi i\mathbf{k}'\cdot\mathbf{x}), \tag{16}$$

respectively. Here it is convenient to regard $\mathbf{x}$ and $\mathbf{k}$ as specifying a geometric ray at the specimen exit surface. Hence $W(\mathbf{x},\mathbf{k})$ specifies the distribution of geometric rays emanating from the specimen exit surface, and $W_{\mathrm{D}}(\mathbf{x},\mathbf{k})$ specifies how these rays 'couple' to the detector *via* the objective postfield. Note that $W_{\mathrm{D}}(\mathbf{x},\mathbf{k})$ contains an incoherent summation over points on the detector, consistent with the incoherent nature of the detection process. A more explicit form for $W_{\mathrm{D}}(\mathbf{x},\mathbf{k})$ is obtained by using equation (13):

$$W_{\mathrm{D}}(\mathbf{x},\mathbf{k}) = \int \mathrm{d}^2\mathbf{k}'\, \tilde{D}(\mathbf{k}')\exp\{2\pi i[\chi(\mathbf{k}+\mathbf{k}'/2)-\chi(\mathbf{k}-\mathbf{k}'/2)]\} \times \exp(2\pi i\mathbf{k}'\cdot\mathbf{x}), \tag{17}$$

where $\tilde{D}(\mathbf{k})$ is the Fourier transform of $D(\mathbf{x})$. In the present language, the detected intensity is given by the overlap of the probe and detector Wigner distributions:

$$I(\mathbf{x}_0) = \int \mathrm{d}^2\mathbf{x}\,\mathrm{d}^2\mathbf{k}\, W_{\mathrm{D}}(\mathbf{x},\mathbf{k})W(\mathbf{x},\mathbf{k},\mathbf{x}_0), \tag{18}$$

where the dependence on the probe position $\mathbf{x}_0$ has been restored simply by noting that the probe state is a function of the probe position.

We reiterate that the formulation contained in equation (18) is a fully wave optical one. On the other hand, if $W_{\mathrm{D}}(\mathbf{x},\mathbf{k})$ is well approximated by a function that takes on values of either 0 or 1 in certain regions of phase space, then a geometric optics interpretation of equation (18) becomes valid. More specifically, $W_{\mathrm{D}}(\mathbf{x},\mathbf{k}) = 1$ will correspond to a geometric ray that emanates from the object plane, passes through the objective postfield and strikes the detector; the strength of this ray will be maintained along its path to the detector, that is, the strength of this ray at the detector will still be $W(\mathbf{x},\mathbf{k},\mathbf{x}_0)$. In contrast, if $W_{\mathrm{D}}(\mathbf{x},\mathbf{k})$ takes on values significantly different from 0 or 1, and, in particular, if it takes on negative values, then such a geometric interpretation of the image formation process is lost.

The geometric optics limit of $W_{\mathrm{D}}(\mathbf{x},\mathbf{k})$ can be obtained in a relatively straightforward manner:

$$\begin{aligned} W_{\mathrm{D}}(\mathbf{x},\mathbf{k}) &= \int \mathrm{d}^2\mathbf{k}'\, \tilde{D}(\mathbf{k}')\exp\{2\pi i[\chi(\mathbf{k}+\mathbf{k}'/2)-\chi(\mathbf{k}-\mathbf{k}'/2)]\} \\ &\quad\times \exp(2\pi i\mathbf{k}'\cdot\mathbf{x}), \\ &\simeq \int \mathrm{d}^2\mathbf{k}'\, \tilde{D}(\mathbf{k}')\exp[2\pi i\mathbf{k}'\cdot(\mathbf{x}+\mathbf{x}(\mathbf{k}))] \\ &= D(\mathbf{x}+\mathbf{x}(\mathbf{k})), \end{aligned} \tag{19}$$

where the essential approximation has been to retain only the first-order term in the following Taylor expansion of the aberration phase shifts about $\mathbf{k}$:

$$\begin{aligned} &\chi(\mathbf{k}+\mathbf{k}'/2)-\chi(\mathbf{k}-\mathbf{k}'/2) \\ &= \mathbf{k}'\cdot\nabla\chi(\mathbf{k}) + \frac{1}{3!}\frac{1}{4}(\mathbf{k}'\cdot\nabla)^3\chi(\mathbf{k}) + \ldots, \end{aligned} \tag{20}$$

and then write $\mathbf{x}(\mathbf{k})$ instead of $\nabla\chi(\mathbf{k})$ [see equation (8)]. [Strictly, this 'first-order derivation' of the geometric limit should be replaced by a more rigorous derivation that uses a so-called uniform approximation to the integral (Berry, 1977). For our purposes, however, the above derivation is adequate.]

For future reference, there are two important scenarios where the higher-order terms in equation (20) vanish and equation (19) holds exactly without approximation, namely, (i) when the aberration function contains only quadratic terms, that is, C_1 and A_1 terms only, and (ii) the small wavelength limit $\lambda \to 0$. As we shall see, equation (19) is also accurate in the case of a sufficiently large detector.

5.1. Application to R-STEM

For R-STEM, we must include aberrations of higher order than C_1 and A_1, and the wavelength must be regarded as finite. In this case, the approximation contained in equation (19) is valid only if the magnitude of the higher-order terms (*i.e.* third-order or greater) in equation (20) is significantly less than unity when $\tilde{D}(\mathbf{k}')$ has an appreciable value. We will then have $\exp[2\pi i(\text{higher-order terms})] \simeq 1$ in equation (19). To obtain an explicit expression of this condition relevant to the present optical geometry, we assume that d is a characteristic dimension of the detector, so that the 'central lobe' of the function $\tilde{D}(\mathbf{k}')$ has width $\sim 2/d$, and assume also that C_n is the dominant higher-order aberration with $n \geq 3$. Consideration of the third-order term in equation (20) then leads to the following condition for the validity of the geometric optics approximation:

$$d \gg \left[\frac{n(n-1)}{24}C_n\lambda^2\beta^n - 2\right]^{1/3}, \tag{21}$$

where β is the scattering angle. Equation (21) says that the geometric optics approximation is valid for a certain minimum detector size, and that the condition for geometric optics becomes stricter as C_n, λ or β increases. The minimum detector size can be interpreted as that which completely encapsulates the 'spreading' of a geometric ray caused by the higher-order aberrations, in which case such spreading has no influence on the detected intensity (see Fig. 6). It should be noted that the condition in equation (21) is a weak condition, in line with the known weak (*i.e.* 'slow') convergence to the geometric (or classical) limit.

For definiteness in the R-STEM case, the ideal image intensity is assumed to be centred at the origin of the image plane. Additionally, we assume that the spatial extent of the ideal image intensity is significantly smaller than the detector geometry. In this case, if d is a characteristic dimension of the detector, only those values of $\mathbf{x}$ for which $|\mathbf{x}| \ll d$ are important in equation (18). Now, from equation (17) it can be inferred that, since the function $\tilde{D}(\mathbf{k})$ has a width $\sim 1/d$, $W_{\mathrm{D}}(\mathbf{x},\mathbf{k}) \simeq W_{\mathrm{D}}(\mathbf{0},\mathbf{k})$ for $|\mathbf{x}| \ll d$. Making this replacement in equation (18), we obtain the following expression valid for a large detector:

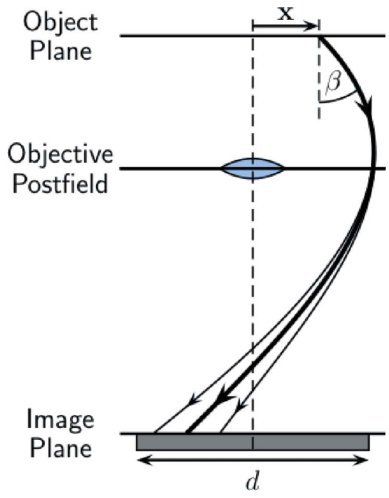

Figure 6
The spreading of a geometric ray (bold line) caused by higher-order aberrations of the objective postfield.

$$I_{\text{R-STEM}}(\mathbf{x}_0) \simeq \int \mathrm{d}^2\mathbf{k}\, W_{\text{D}}(\mathbf{0},\mathbf{k}) \int \mathrm{d}^2\mathbf{x}\, W(\mathbf{x},\mathbf{k},\mathbf{x}_0) = \int \mathrm{d}^2\mathbf{k}\, W_{\text{D}}(\mathbf{0},\mathbf{k}) I(\mathbf{k},\mathbf{x}_0), \quad (22)$$

where $I(\mathbf{k},\mathbf{x}_0)$ is the intensity in the diffraction plane. Equation (22) can be evaluated using either wave or geometric optics depending on whether $W_{\text{D}}(\mathbf{0},\mathbf{k})$ is taken from equation (17) or equation (19), respectively. If evaluated using wave optics, the real (but not necessarily positive) function $W_{\text{D}}(\mathbf{0},\mathbf{k})$ can be regarded as the effective detector function operating in the diffraction plane in the wave optics theory. To emphasize the role of this function it will be denoted by $\mathcal{D}(\mathbf{k})$. It is given explicitly by the expression

$$\mathcal{D}(\mathbf{k}) = \int \mathrm{d}^2\mathbf{k}'\, \tilde{D}(\mathbf{k}') \exp\{2\pi i[\chi(\mathbf{k}+\mathbf{k}'/2) - \chi(\mathbf{k}-\mathbf{k}'/2)]\}. \quad (23)$$

On the other hand, if evaluated according to geometric optics, the function $W_{\text{D}}(\mathbf{0},\mathbf{k})$ is just the effective detector function

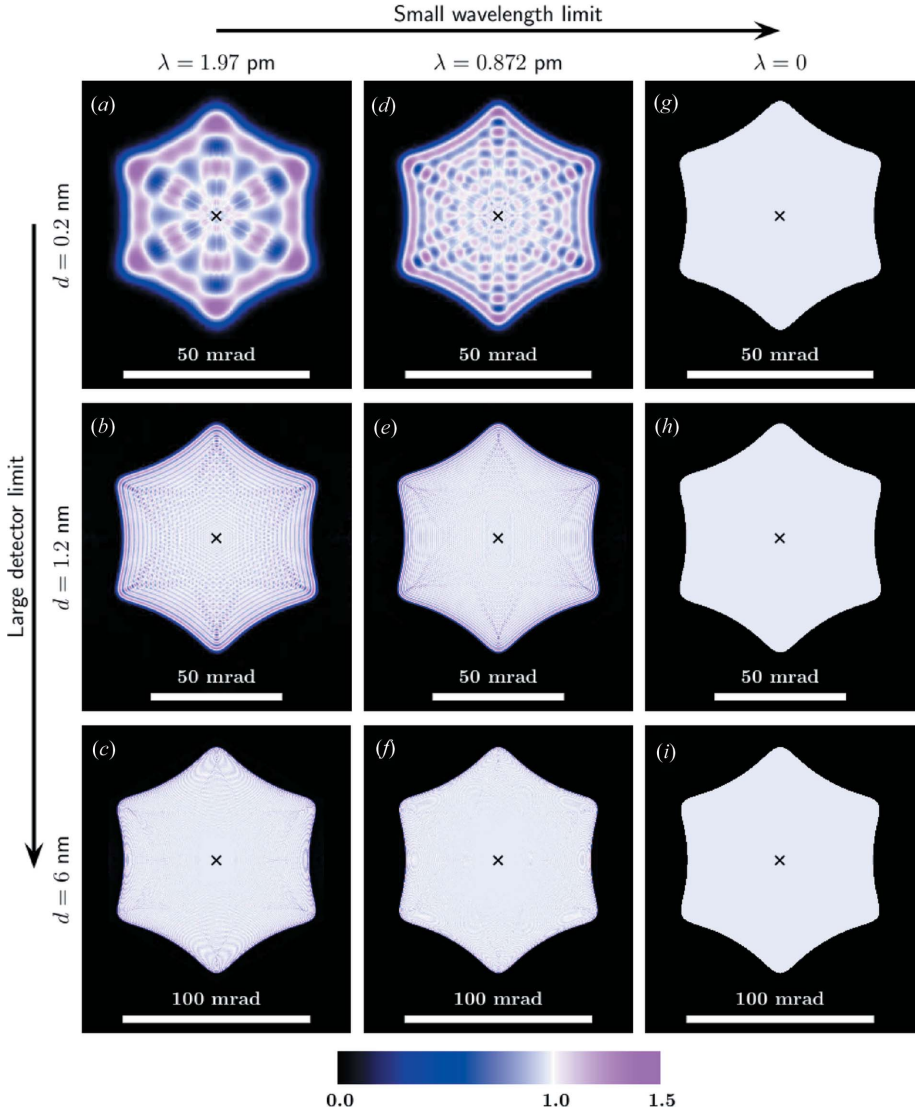

Figure 7
Comparison of wave optics (*a*)–(*f*) and geometric optics (*g*)–(*i*) effective detector functions for disc-shaped image-plane detectors of different diameters (indicated on the left). Wave optics results are shown for wavelengths $\lambda = 1.97$ pm (*a*)–(*c*) and $\lambda = 0.872$ pm (*d*)–(*f*), corresponding to electron beam energies of 300 keV and 1 MeV, respectively. All figures assume aberration coefficients of $C_5 = 6.8$ mm and $|A_5| = 3.1$ mm. The apparent hexagonal shapes are caused by the A_5 aberration. Crosses mark the centre of the diffraction plane. The intensity scale at the bottom applies to all subfigures.

$D(\mathbf{x}(\mathbf{k}))$ introduced in §4, and equation (22) is then identical to equation (11).

A comparison of the effective detector functions $\mathcal{D}(\mathbf{k})$ and $D(\mathbf{x}(\mathbf{k}))$ illuminates the validity of the geometric optics approximation in R-STEM. Fig. 7 shows such a comparison for disc-shaped image-plane detectors of different sizes and for different electron wavelengths. The wave optics effective detectors (Figs. 7*a*–7*f*) exhibit the characteristic 'Airy form' (Berry, 1977), oscillating in the geometrically allowed region (indicating wave interference) and decaying exponentially in the geometrically forbidden region. This behaviour is especially clear in Figs. 7(*a*) and 7(*b*), but it is also present, though more difficult to discern, in Figs. 7(*c*)–7(*f*). In contrast, the geometric optics effective detectors (Figs. 7*g*–7*i*) contain no such oscillations because $D(\mathbf{x}(\mathbf{k}))$ can only take on a value of 1 or 0, as discussed above. The results in Fig. 7 demonstrate clearly how the oscillations in the wave optics effective detector become smaller and more closely spaced with increasing detector size, leading to better agreement with the geometric optics result. From equation (23) this behaviour can be understood as a narrowing of the function $\tilde{D}(\mathbf{k})$, so that the first-order Taylor expansion in equation (20) leading to the geometric optics expression becomes a more accurate approximation, as discussed above. A similar trend towards geometric optics is observed in connection with the small wavelength limit, as expected. In Fig. 7 it can also be seen that the magnitude of the oscillations indicative of the breakdown of geometric optics increases with scattering angle, in agreement with the behaviour expected from equation (21).

The detector size corresponding to the transition from wave to geometric optics, as seen in Fig. 7, can be predicted by recognizing that, when the spatial extent of the ideal image intensity is significantly smaller than the detector, equation (21) need hold only for a restricted range of scattering angles. From Fig. 7, it can be recognized that the largest important scattering angle corresponds roughly to that of a geometric ray which is displaced to the edge of the detector, *i.e.* $\beta = (d/2C_n)^{1/n}$. Substituting this value into equation (21), we obtain, after some algebra,

$$d \gg \left[2\left(\frac{n(n-1)}{48}\right)^{n/2} C_n \lambda^n\right]^{1/(n+1)}. \qquad (24)$$

Table 1 shows the value of the right-hand side of equation (24) for aberration coefficients relevant to C_3-dominated and C_3-corrected objective lenses. The row labelled '$C_5 = 10$ mm' in Table 1 is applicable to the first column in Fig. 7. Hence equation (24) says that the geometric optics approximation should hold for detectors significantly larger than about 0.06 nm, in adequate agreement with the first column in Fig. 7.

Notwithstanding the remarks above, it should be remembered that the R-STEM intensity involves an integration over the diffraction plane. Hence, even when $\mathcal{D}(\mathbf{k})$ contains appreciable oscillations, the geometric optics approximation may still provide sufficient accuracy, though this will depend on whether or not the specific form of the scattered intensity $I(\mathbf{k}, \mathbf{x}_0)$ affords sufficient averaging over the oscillations.

Table 1
The approximate lower bound on the detector size for the validity of the geometric optics approximation in R-STEM, as given by equation (24), for aberration coefficients representative of C_3-dominated and C_3-corrected objective lenses.

A beam energy of 300 keV is assumed.

Aberration	Right-hand side of equation (24) (nm)
$C_3 = 1$ mm	0.16
$C_5 = 10$ mm	0.063
$C_7 = 100$ mm	0.044

Finally, in reference to Fig. 7, the assumption that the detector geometry is larger than the extent of the ideal image is, in a practical scenario, likely to break down for the 0.2 nm detector (and possibly the 1.2 nm detector too). However, this does not affect the present conclusions regarding the validity of the geometric optics approximation in R-STEM because the former assumption is independent of the geometric optics approximation.

5.2. Application to SCEM

For SCEM, we assume that an angle-limiting aperture circumvents higher-order aberrations. (If no aperture is used then we must include higher-order aberrations and the considerations of the previous section apply.) If we can neglect higher-order aberrations on account of the aperture, then the condition equation (21) is vacuous (since we can assume $C_n \simeq 0$ for $n \geq 3$). However, diffraction from the aperture limits the validity of a geometric interpretation of image formation. To this end, the relevant Wigner distribution involves that of a circular aperture, for which an approximate closed form has been derived (Bastiaans & van de Mortel, 1996; Yang & Lang, 2005). Assuming the detector is a pinhole centred on the optic axis, we can obtain a Wigner distribution describing image formation in SCEM:

$$\begin{aligned} W_{\mathrm{A}}(\mathbf{x}, \mathbf{k}) &= \int \mathrm{d}^2\mathbf{k}'\, \overline{A}(\mathbf{k} - \mathbf{k}'/2) A(\mathbf{k} + \mathbf{k}'/2) \\ &\quad \times \exp[2\pi i \mathbf{k}' \cdot (\mathbf{x} + \mathbf{x}(\mathbf{k}))] \\ &\simeq \mathrm{OTF}_{a/2}(\mathbf{k}) \mathrm{CTF}_{2a}(\tilde{\mathbf{x}} + \tilde{\mathbf{x}}(\mathbf{k})), \end{aligned} \qquad (25)$$

where $A(\mathbf{k})$ is the transmission function for an aperture of radius a, $\mathrm{OTF}_a(\mathbf{k})$ is the well known (Goodman, 1968) incoherent optical transfer function,

$$\mathrm{OTF}_a(\mathbf{k}) = \frac{2}{\pi}\left\{\cos^{-1}\frac{|\mathbf{k}|}{2a} - \frac{|\mathbf{k}|}{2a}\left[1 - \left(\frac{|\mathbf{k}|}{2a}\right)^2\right]^{1/2}\right\} \qquad (26)$$

and $\mathrm{CTF}_a(\mathbf{x})$ is the well known (Goodman, 1968) coherent transfer function in real space,

$$\mathrm{CTF}_a(\mathbf{x}) = \frac{aJ_1(2\pi a|\mathbf{x}|)}{|\mathbf{x}|}. \qquad (27)$$

In equation (25), $\tilde{\mathbf{x}}$ denotes the scaled position vector $\{(a - |\mathbf{k}|/a)x, [(a^2 - |\mathbf{k}|^2)^{1/2}/a]y\}$, where the x axis coincides with $\hat{\mathbf{k}}$. The form of the coherent transfer function implies that a geometric ray originating from the object plane will be

'spread' across the image plane as a consequence of diffraction from the aperture. Moreover, the oscillatory nature of the coherent transfer function means that the strength of the ray will be reversed in some parts of the image plane. As discussed above, this behaviour indicates the breakdown of the geometric interpretation.

In contrast to such behaviour, an application of the small-wavelength limit (Berry, 1977; Filippas & Makrakis, 2003) to equation (25) yields the Boolean function

$$W_{\rm A}^{\lambda=0}(\mathbf{x},\boldsymbol{\beta}) = \lim_{\lambda\to 0}\frac{1}{\lambda^2}W_{\rm A}(\mathbf{x},\boldsymbol{\beta}/\lambda) = A(\boldsymbol{\beta})\delta(\mathbf{x}+\mathbf{x}(\boldsymbol{\beta})), \quad (28)$$

where $\boldsymbol{\beta} = \lambda\mathbf{k}$ (the use of $\boldsymbol{\beta}$ in connection with the small-wavelength limit avoids the implicit dependence on λ contained in $\mathbf{k}$). Equation (28) implies simply that a geometric ray will contribute to the final SCEM image if it passes through the aperture and strikes the pinhole detector.

Reconciliation of geometric optics and SCEM can be achieved by noting that, in reality, the detector size d is finite. As was the case for R-STEM, a sufficiently large detector will encapsulate the spreading of a geometric ray, which is now caused by diffraction from the aperture. In a manner similar to that described for R-STEM, we specify that the detector should at least encapsulate the central lobe of the coherent transfer function, leading to the condition

$$d \gg \frac{\lambda}{2(\beta_{\rm max}-\beta)}, \qquad (\beta<\beta_{\rm max}), \quad (29)$$

with $\beta_{\rm max}$ denoting the aperture semi-angle. Hence, if this condition is satisfied, we can write, approximately,

$$W_{\rm A}(\mathbf{x},\mathbf{k}) \simeq A(\mathbf{k})D(\mathbf{x}+\mathbf{x}(\mathbf{k})), \quad (30)$$

which has the same interpretation as equation (28) except that the detector size is now finite. From equation (29) we infer that a geometric interpretation of image formation in SCEM can only apply to the subset of geometric rays that do not pass 'too close' to the edge of the aperture. This picture appears consistent with a geometrical theory of diffraction (Keller, 1962).

6. Conclusions

In summary, we have considered image formation in STEM using object-conjugate detectors, a geometry that encompasses the three-dimensional imaging technique of SCEM and the recently developed atomic resolution imaging technique of R-STEM. Image formation in this optical geometry was considered from the perspectives of wave optics and geometric optics. For the case of aberration-corrected SCEM, where the use of an angle-limiting aperture means that aberrations other than C_1 and A_1 can often be ignored, a Wigner distribution analysis demonstrated that wave and geometric optics provide equivalent descriptions of the image formation process, provided that the detector is large enough to average out the effects of diffraction from the angle-limiting aperture. In the case of R-STEM, which was the primary focus of this article, it was shown that a naive application of wave optics can place excessive demands on computational resources on account of the dense sampling required to describe the higher-order postfield aberrations. It was also demonstrated that the image formation portion of the R-STEM optics can be accurately described by geometric optics, provided that the detector is large enough to average out 'diffraction' caused by higher-order aberrations. In addition to being computationally more efficient than wave optics, the resulting geometrical theory of R-STEM also enables a conceptually simple interpretation in terms of an effective detector operating in the diffraction plane. Finally, the geometric optics theory of R-STEM was shown to be in good agreement with experimental images of $SrTiO_3$. Such agreement, in addition to that reported earlier (Lazar *et al.*, 2011) for images of LaB_6, provides substantial confidence in its validity.

References

Allen, L. J., Findlay, S. D., Oxley, M. P. & Rossouw, C. J. (2003). *Ultramicroscopy*, **96**, 47–63.

Bastiaans, M. J. (1997). *The Wigner Distribution – Theory and Applications in Signal Processing*, edited by W. Mecklenbräuker & F. Hlawatsch, pp. 375–426. Amsterdam: Elsevier Science.

Bastiaans, M. J. & van de Mortel, P. G. J. (1996). *J. Opt. Soc. Am. A*, **13**, 1698–1703.

Berry, M. V. (1977). *Philos. Trans. R. Soc. London Ser. A*, **287**, 237–271.

Castano, V. (1989). *Computer Simulation of Electron Microscopy Diffraction and Images*, edited by W. Krakow & M. O'Keefe, p. 33. Pennsylvania, USA: The Minerals, Metals and Materials Society.

Chang, L. Y., Kirkland, A. I. & Titchmarsh, J. (2006). *Ultramicroscopy*, **106**, 301–306.

Dwyer, C. (2010). *Ultramicroscopy*, **110**, 195–198.

Dwyer, C., Erni, R. & Etheridge, J. (2008). *Appl. Phys. Lett.* **93**, 021115.

Dwyer, C., Erni, R. & Etheridge, J. (2010). *Ultramicroscopy*, **110**, 952–957.

Etheridge, J., Lazar, S., Dwyer, C. & Botton, G. A. (2011). *Phys. Rev. Lett.* **106**, 160802.

Filippas, S. & Makrakis, G. N. (2003). *Multiscale Model. Simul.* **1**, 674–710.

Findlay, S. D., Allen, L. J., Oxley, M. P. & Rossouw, C. J. (2003). *Ultramicroscopy*, **96**, 65–81.

Frigo, S. P., Levine, Z. H. & Zaluzec, N. J. (2002). *Appl. Phys. Lett.* **81**, 2112–2114.

Goodman, J. W. (1968). *Introduction to Fourier Optics*. San Francisco: McGraw Hill Book Company.

Goodman, P. & Moodie, A. F. (1974). *Acta Cryst.* A**30**, 280–290.

Haider, M., Uhlemann, S., Schwan, E., Rose, H., Kabius, B. & Urban, K. (1998). *Nature (London)*, **392**, 768–769.

Ishizuka, K. (2002). *Ultramicroscopy*, **90**, 71–83.

Kainuma, Y. (1955). *Acta Cryst.* **8**, 247–257.

Keller, J. B. (1962). *J. Opt. Soc. Am.* **52**, 116–130.

Kirkland, E. J. (2010). *Advanced Computing in Electron Microscopy*, 2nd ed. New York: Plenum Press.

Kirkland, E. J., Loane, R. F. & Silcox, J. (1987). *Ultramicroscopy*, **23**, 77–96.

Krivanek, O. L., Dellby, N. & Lupini, A. R. (1999). *Ultramicroscopy*, **78**, 1–11.

Lazar, S., Etheridge, J., Dwyer, C., Freitag, B. & Botton, G. A. (2011). *Acta Cryst.* A**67**, 487–490.

LeBeau, J. M., Findlay, S. D., Allen, L. J. & Stemmer, S. (2008). *Phys. Rev. Lett.* **100**, 206101.

Loane, R. F., Xu, P. & Silcox, J. (1991). *Acta Cryst.* A**47**, 267–278.

Loane, R. F., Xu, P. & Silcox, J. (1992). *Ultramicroscopy*, **40**, 121–138.
Maunders, C., Dwyer, C., Tiemeijer, P. C. & Etheridge, J. (2011). *Ultramicroscopy*, **111**, 1437–1446.
Mitsuishi, K., Hashimoto, A., Takeguchi, M., Shimojo, M. & Ishizuka, K. (2010). *Ultramicroscopy*, **111**, 20–26.
Nellist, P. D., Behan, G., Kirkland, A. I. & Hetherington, C. J. D. (2006). *Appl. Phys. Lett.* **89**, 124105.
Nellist, P. D. & Pennycook, S. J. (2000). *Adv. Imag. Electr. Phys.* **113**, 147–203.
Pennycook, S. J. & Boatner, L. A. (1988). *Nature* (*London*), **336**, 565–567.
Press, W. H., Teukolsky, S. A., Vetterling, W. T. & Flannery, B. P. (2002). *Numerical Recipies in C++: the Art of Scientific Computing*, 2nd ed. Cambridge University Press.
Rossouw, C. J., Allen, L. J., Findlay, S. D. & Oxley, M. P. (2003). *Ultramicroscopy*, **96**, 299–312.
Schattschneider, P., Nelhiebel, M. & Jouffrey, B. (1999). *Phys. Rev. B*, **59**, 10959–10969.
Stadelmann, P. (2004). http://cimewww.epfl.ch/people/stadelmann/jemsWebSite/jems.html.
Takeguchi, M., Hashimoto, A., Shimojo, M. & Furuya, K. (2008). *J. Electron Microsc.* **57**, 123–127.
Torre, A. (2005). *Linear Ray and Wave Optics in Phase Space.* The Netherlands: Elsevier B.V.
Uhlemann, S. & Haider, M. (1998). *Ultramicroscopy*, **72**, 109–119.
Verbeeck, J., Schattschneider, P. & Rosenauer, A. (2009). *Ultramicroscopy*, **109**, 350–360.
Wang, P., Behan, G., Kirkland, A. I., Nellist, P. D., Cosgriff, E. C., D'Alfonso, A., Morgan, A. J., Allen, L. J., Hashimoto, A., Takeguchi, M., Mitsuishi, K. & Shimojo, M. (2011). *Ultramicroscopy*, **111**, 877–886.
Yang, Q., Liu, L. & Lang, H. (2005). *J. Opt. A Pure Appl. Opt.* **7**, 431–437.